Pergamon

Int. J. Heat Mass Transfer. Vol. 37, No. 9, pp. 1401–1409, 1994

0017-9310/94 $7.00+0.00

0017-9310(93)E0086-V

Transient deformation and evaporation of droplets at intermediate Reynolds numbers

R. J. HAYWOOD, M. RENKSIZBULUT† and G. D. RAITHBY
University of Waterloo, Mechanical Engineering Department, Waterloo, Ontario, Canada N2L 3G1

(*Received* 5 *February* 1993 *and in final form* 9 *November* 1993)

Abstract—The early life histories of isolated *n*-heptane droplets injected into 1000 K air at 1 and 10 atm with initial Reynolds and Weber numbers of 100 and 2, respectively, are reported. A numerical model is used to predict the transient droplet shape, and the velocity, pressure, temperature and concentration fields in both phases. Initially spherical droplets show strongly damped oscillations at frequencies within 25% of the theoretical natural frequency of Lamb (1932). Circulation within the droplets is responsible for the observed strong damping and promotes the formation of prolate shapes for surfactant-free droplets. The computed heat and mass transfer rates are well predicted by existing quasi-steady correlations.

INTRODUCTION

PRACTICAL interest in the evaporation and combustion of liquid fuel sprays has naturally led to the need for a detailed understanding of the convective vaporization of droplets in high temperature environments at intermediate Reynolds numbers ($Re = O(100)$). Extensive reviews of the related literature have been conducted by Law [1], Faeth [2], Sirignano [3], and Dwyer [4]. More recent studies (Prakash and Sirignano [5], Renksizbulut and Yuen [6], Dwyer and Sanders [7], Renksizbulut and Haywood [8], Haywood *et al.* [9], Huang and Ayyaswamy [10], Chiang *et al.* [11]), have addressed the effects of gas and liquid phase transients, variable thermophysical properties, and liquid phase heat and momentum transport, thereby eliminating most of the limiting assumptions that were made in early analyses of droplet evaporation.

One assumption that yet prevails is that droplets maintain spherical shapes. However, consider the parameters typical of a droplet within a hydrocarbon spray issuing into a combustion chamber: $T^*_\infty \approx 1000$ K, $p^*_\infty \approx 10$ atm, $\rho^*_\infty \approx 4$ kg m^{-3}, $U^*_{REL} \approx 10$ m s^{-1}, $d^*_o \approx 100$ μm, $T^*_{l,o} \approx 300$ K, $\gamma^* \approx 0.020$ N m^{-1}, and $\mu^*_\infty \approx 3.5 \times 10^{-5}$ kg m^{-1} s^{-1}. These yield an initial Reynolds number of 114, and an initial Weber number of 2. Experimental and theoretical studies (Clift *et al.* [12]) indicate that droplets at this Weber number are appreciably non-spherical. After the droplet is injected into the combustion chamber, the Weber number will obviously decay from this initial value as the droplet decelerates under the influence of aerodynamic drag. At the same time, however, the rising surface temperature will reduce the interfacial tension and at least partially offset the velocity effect. Hence, the effects of droplet deformation on the heat, mass, and momentum transfer rates of convecting evaporating droplets must be determined.

One of the pioneering studies on non-spherical droplet dynamics is the work of Lamb [13] who derived the following expression for the natural frequency of infinitesimal amplitude oscillations of an inviscid droplet immersed in an inviscid quiescent second fluid:

$$\omega^* = \frac{1}{2\pi}\left(\frac{192\gamma^*}{(3\rho^*_1+2\rho^*_2)d^{*3}_o}\right)^{1/2}. \quad (1)$$

Extensions of this work provided expressions for the frequency and damping rate of fluid droplets in terms of droplet size and fluid properties while including the effects of finite viscosities (Miller and Scriven [14]) and creeping flow in the continuous phase (Subramanyam [15]). In general, the theoretical analysis of the motion of deforming bubbles and drops has only been possible in limiting situations such as inviscid or highly viscous fluids and/or nearly spherical droplets (Harper [16]).

Recent advances in numerical methods have provided a means to solve non-spherical droplet problems at intermediate Reynolds numbers (Miksis *et al.* [17], Ryskin and Leal [18], Christov and Volkov [19], Dandy and Leal [20]). Unfortunately, none of these studies include the parametric ranges $\mu_1/\mu_2 \approx 10$ and $\rho_1/\rho_2 \approx 100$, nor do they consider the effects of transients (including transient droplet deformation), variable thermophysical properties, or heat and mass transfer. An exception is the recent work of Deng *et al.* [21] who have studied the evaporation and deformation of droplets at high temperatures and pressures.

Presently, there exists a wealth of experimental data regarding the motion of deforming bubbles and drops (Grace [22] and Grace *et al.* [23]) not all of which are

†Please address all correspondence to M. Renksizbulut.

NOMENCLATURE

A	nondimensional area, A^*/R_o^{*2}
B_H	heat transfer number, $c_{P,g}^*(T_\infty^* - T_s^*)(1-Q_l/Q_g)/L_s^*$
B_M	mass transfer number, $(Y_{F,s} - Y_{F,\infty})/(1 - Y_{F,s})$
c_P	specific heat at constant pressure, $c_P^*/c_{P,\infty}^*$
C_D	total drag coefficient, $2F_D^*/(\pi R^{*2}\rho_\infty^* U_\infty^{*2})$
d^*	diameter of volume equivalent sphere
$\mathscr{D}_{FA}$	species diffusion coefficient, $\mathscr{D}_{FA}^*/\mathscr{D}_{FA,\infty}^*$
$\hat{e}$	unit vector
Eo	Eötvös number, $g^* d^* \rho_l^* / \gamma^*$
F^*	force
g^*	gravitational acceleration
h_H^*	heat transfer coefficient
h_M^*	mass transfer coefficient
H	mean curvature, $-R_o^*(1/r_1^* + 1/r_2^*)/2$
$\tilde{I}$	identity tensor
k	thermal conductivity, k^*/k_∞^*
L_s	enthalpy of vaporization, $L_s^*/(c_{P,\infty}^* T_\infty^*)$
m^*	mass
$\dot{m}^*$	total evaporation rate
$\dot{m}''$	local mass flux, $\dot{m}''^*/(\rho_\infty^* U_{\infty,o}^*)$
$\hat{n}$	unit normal vector
Nu	Nusselt number, $h_H^* d^*/k^*$
p_g	gas pressure, $(p_g^* - p_\infty^*)/(\rho_\infty^* U_{\infty,o}^{*2})$
p_l	liquid pressure, $(p_l^* + \rho^* x^* \mathrm{d}U_\infty^*/\mathrm{d}t^* - 2\gamma_o^*/R_o^* - p_\infty^*)/(\rho_\infty^* U_{\infty,o}^{*2})$
Pr	Prandtl number, $\mu^* c_P^*/k^*$
Q^*	heat transfer rate
r_1^*, r_2^*	principle radii of curvature
R^*	radius of equivalent volume sphere
Re	Reynolds number, $2R^*\rho_\infty^* U_\infty^*/\mu^*$
Re_m	film Reynolds number, $2R^*\rho_\infty^* U_\infty^*/\mu_f^*$
Sh	Sherwood number, $h_M^* d^*/(\rho^* \mathscr{D}_{FA}^*)$
Sc	Schmidt number, $\mu^*/(\rho^* \mathscr{D}_{FA}^*)$
t	time, $t^* U_{\infty,o}^*/R_o^*$
$\hat{t}$	unit tangent vector
T	temperature, T^*/T_∞^*
u	velocity component in x direction, $u^*/U_{\infty,o}^*$
U_∞^*	instantaneous free stream velocity
v	velocity component in y direction, $v^*/U_{\infty,o}^*$
V	volume, V^*/R_o^{*3}
We	Weber number, $\rho_\infty^* U_\infty^{*2} d^*/\gamma^*$
x	axial distance in cylindrical coordinates, x^*/R_o^*
X	mole fraction
y	radial distance in cylindrical coordinates, y^*/R_o^*
Y	mass fraction.

Greek symbols

α	aspect ratio; $\alpha > 1$ for oblate shapes
γ	surface tension, γ^*/γ_o^*
μ	viscosity, μ^*/μ_∞^*
ρ	density, ρ^*/ρ_∞^*
$\tilde{\sigma}$	viscous stress tensor, $\tilde{\sigma}^*(R_o^*/\mu_\infty^* U_{\infty,o}^*)$
ω	oscillation frequency, $\omega^* R_o^*/U_{\infty,o}^*$

Subscripts and superscripts

Λ	unit vector
$\rightarrow$	vector
$\sim$	tensor
*	dimensional quantity
$-$	spatial average
1, 2	dispersed, continuous phase
∞	free stream conditions
A	air
f	film conditions
F	fuel
g	gas phase
l	liquid phase
o	initial value
s	at the droplet surface
T	transpose.

relevant to spray evaporation. Garner and Lane [24] studied the shapes, oscillations, and internal circulation of drops of 15 different liquids falling at their terminal velocities in air, and in air/carbon-dioxide mixtures. Droplet aspect ratios were found to be linearly dependent on the Eötvös number such that $\alpha = 1.0 + 0.125Eo$ for $Eo < 9$. Oscillation frequencies were found to agree with the theoretical predictions of Lamb [13]. Winnikow and Chao [25] and Thorsen *et al.* [26] have examined the behavior of droplets falling at terminal velocities for systems of exceptional purity. Drag coefficients were found to be considerably lower than the corresponding rigid sphere drag, and lower than other published data for the same fluids. The reduced drag was attributed to a reduction in friction drag due to vigorous internal circulation. It appears that contaminated systems do not allow the development of internal circulation to the same degree as pure systems. The physical mechanism thought to be responsible for this behavior is the surface-active material forming a surface-tension gradient that opposes the shear stress imparted by the continuous phase.

Studies on precipitation and cloud physics (Magono [27], McDonald [28], Reinhart [29], Pruppacher and Beard [30]) have led to great insight into

the fluid mechanics of spherical and deformed water droplets falling at terminal velocity in air, for which the thermophysical property ratios are similar to those of hydrocarbon/air systems. Equilibrium shapes are generally found to be flattened oblate ellipsoids satisfying a balance between the major interfacial normal stresses (i.e. externally: surface tension and aerodynamic pressure, and internally: hydrostatic pressure). The effects of liquid motion were discerned by Foote [31] who showed that internal circulation contributes not only to stresses that can be comparable in magnitude to those previously mentioned (surface tension, aerodynamic, hydrostatic) but that the effect of the liquid motion is to reduce the flattening of droplets. A recent theoretical analysis by Petrov [32] supports these conclusions.

The motivation for the present work is to remove a major limitation of practically all current theoretical investigations of convective fuel droplet dynamics and energetics: the assumption of spherical shape. The following specific issues will be addressed. (1) What are the oscillation frequencies, amplitudes, and damping rates of typical fuel droplets? (2) What are the effects of droplet deformation on heat, mass and momentum transfer rates? (3) What are the effects of droplet deformation on liquid phase motion and liquid phase heating? The second question has been at least partially addressed in a recent paper by Haywood *et al.* [33] wherein calculations were made of the steady shape, heat, mass, and momentum transfer rates of typical fuel droplets over a range of Reynolds and Weber numbers. The emphasis of the current work is on the transient behavior of fuel droplets injected into high temperature air, and seeks to determine the duration and effects of the early oscillatory behavior.

FORMULATION

Under investigation is the transient behavior (including deformation and evaporation) of an isolated droplet of a typical hydrocarbon fuel injected into a quiescent hot gaseous environment. The problem is shown schematically in Fig. 1. In the formulation of the mathematical model it has been assumed that: (1) the droplet maintains an axisymmetric shape, (2) the flow field is laminar and axisymmetric, (3) there are no external body forces, (4) thermal radiation, viscous dissipation, and second order mass and energy diffusion effects (i.e. Soret and Dufour effects and pressure diffusion) are negligible, (5) thermodynamic equilibrium prevails at the gas/liquid interface, (6) air is insoluble in the liquid droplet, and (7) the liquid/gas interface is free of surface-active agents. All effects due to liquid phase motion and heating, and transient variations in droplet shape, size, and velocity are included in the analysis. Temperature and concentration dependence of all thermophysical properties are considered (see Haywood [34]) with the exception of the liquid phase density which is assumed to be constant. A reference frame moving with the droplet at a velocity U_G is adopted. The governing equations are non-dimensionalized as defined in the Nomenclature section, and they are concisely presented in Table 1. The equations have been cast into a control-volume form through the use of Liebnitz's rule and Gauss's divergence theorem. The dimensionless boundary conditions are:

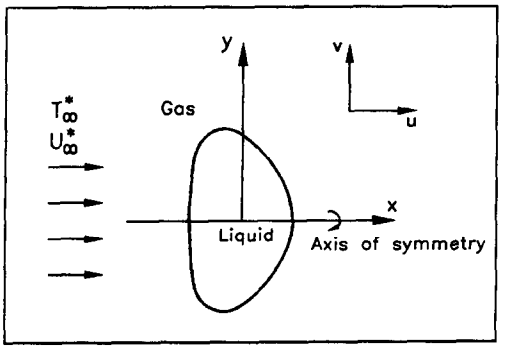

FIG. 1 Problem schematic.

- At the liquid/gas interface:

(i) temperature is single valued,

$$T_l = T_g \tag{2}$$

(ii) energy is conserved,

$$-(k\vec{\nabla}T\cdot\hat{n})_l = -(k\vec{\nabla}T\cdot\hat{n})_g + \frac{Re_{\infty,o}Pr_\infty}{2}\dot{m}''L_s \tag{3}$$

(iii) air is insoluble in the liquid phase, leading to:

$$\dot{m}'' = \frac{2}{Re_{\infty,o}Sc_\infty}\left(\frac{\rho\mathscr{D}_{FA}}{(1-Y_F)}\vec{\nabla}Y_F\cdot\hat{n}\right)_g \tag{4}$$

(iv) the fuel mole fraction is determined by the vapour pressure at T_s,

$$X_F = p^*_F(T^*_s)/p^*_\infty \tag{5}$$

(v) conservation of mass,

$$\rho(\vec{v}-\vec{v}_s)\cdot\hat{n}|_l = \rho(\vec{v}-\vec{v}_s)\cdot\hat{n}|_g \tag{6}$$

(vi) there is no slip between the phases,

$$\vec{v}\cdot\hat{t}|_l = \vec{v}\cdot\hat{t}|_g \tag{7}$$

(vii) continuity of stress,

$$\left[\rho\vec{v}(\vec{v}-\vec{v}_s)+p\tilde{I}-\frac{2}{Re_{\infty,o}}\tilde{\sigma}\right]\cdot\hat{n}|_l = \left[\rho\vec{v}(\vec{v}-\vec{v}_s)+p\tilde{I}-\frac{2}{Re_{\infty,o}}\tilde{\sigma}\right]\cdot\hat{n}|_g + \left(\frac{-4}{We_{\infty,o}}(\gamma H+1)-\rho_l\frac{dU_\infty}{dt}x\right)\hat{n}-\frac{2}{We_{\infty,o}}\vec{\nabla}_s\gamma \tag{8}$$

where:

Table 1. The non-dimensional governing equations

$$\frac{\mathrm{d}}{\mathrm{d}t}\int_{\mathrm{V}}\rho\phi\,\mathrm{d}V+\int_{\mathrm{S}}\rho(\vec{v}-\vec{v}_{\mathrm{S}})\cdot\hat{n}\phi\,\mathrm{d}A=\int_{\mathrm{S}}\Gamma_{\phi}\vec{\nabla}\phi\cdot\hat{n}\,\mathrm{d}A+S_{\phi}$$

Equation	ϕ	Γ_{ϕ}	S_{ϕ}
Continuity	1	0	S_C
Axial momentum	u	$2\mu/Re_{\infty,0}$	S_u
Radial momentum	v	$2\mu/Re_{\infty,0}$	S_v
Energy	T	$2k/(c_{\mathrm{P}}Re_{\infty,0}Pr_{\infty})$	S_E
Species	Y_{F}	$2\rho\mathscr{D}_{\mathrm{FA}}/(Re_{\infty,0}Sc_{\infty})$	S_Y

$$S_C=S_Y=0$$

$$S_u\dagger=\frac{2}{Re_{\infty,0}}\int_{\mathrm{S}}(\vec{\sigma}\cdot\hat{n}\cdot\hat{e}_x-\mu\vec{\nabla}u\cdot\hat{n})\,\mathrm{d}A+\int_{\mathrm{V}}\left(-\vec{\nabla}p\cdot\hat{e}_x+\rho\frac{\mathrm{d}U_{\infty}}{\mathrm{d}t}\right)\mathrm{d}V$$

$$S_v=\frac{2}{Re_{\infty,0}}\int_{\mathrm{S}}(\vec{\sigma}\cdot\hat{n}\cdot\hat{e}_y-\mu\vec{\nabla}v\cdot\hat{n})\,\mathrm{d}A+\int_{\mathrm{V}}(-\vec{\nabla}p\cdot\hat{e}_y)\,\mathrm{d}V$$

$$S_E=\int_{\mathrm{V}}\left[\frac{2}{Re_{\infty,0}Pr_{\infty}}\frac{k}{c_{\mathrm{P}}^2}(\vec{\nabla}T\cdot\vec{\nabla}c_{\mathrm{P}})+\frac{2}{Re_{\infty,0}Sc_{\infty}}\left(\frac{c_{\mathrm{P,F}}-c_{\mathrm{P,A}}}{c_{\mathrm{P}}}\right)\rho\mathscr{D}_{\mathrm{FA}}(\vec{\nabla}T\cdot\vec{\nabla}Y_{\mathrm{F}})\right]\mathrm{d}V.$$

† Due to non-dimensionalization, $\rho\,\mathrm{d}U_{\infty}/\mathrm{d}t$ appears in the gas phase S_u only.

$$\vec{\sigma}=\mu\left[\vec{\nabla}\vec{v}+(\vec{\nabla}\vec{v})^{\mathrm{T}}-\frac{2}{3}\vec{\nabla}\cdot\vec{v}\vec{I}\right]$$

- At the free stream inlet:

$$T=1,\quad Y_{\mathrm{F}}=0,\quad u=U_{\infty},\quad v=0 \tag{9}$$

- At the free stream outlet:

$$\partial\phi/\partial x=0;\quad \phi=u,v,T,Y_{\mathrm{F}} \tag{10}$$

- Along the axis of symmetry:

$$v=0,\quad \partial\phi/\partial y=0;\quad \phi=u,T,Y_{\mathrm{F}}. \tag{11}$$

The dimensionless heat transfer coefficient (Nusselt number) and mass transfer coefficient (Sherwood number) are calculated as:

$$Nu_{\infty}=\frac{(m/m_0)^{1/3}}{\int_{\mathrm{S}}\mathrm{d}A}\int_{\mathrm{S}}\frac{k\vec{\nabla}T\cdot\hat{n}}{(1-T_{\mathrm{S}})}\mathrm{d}A \tag{12}$$

$$Sh_{\infty}=\frac{(m/m_0)^{1/3}}{\int_{\mathrm{S}}\mathrm{d}A}\int_{\mathrm{S}}\frac{\rho\mathscr{D}_{\mathrm{FA}}\vec{\nabla}Y\cdot\hat{n}}{(Y_{\mathrm{F},\infty}-Y_{\mathrm{F,S}})}\mathrm{d}A. \tag{13}$$

A finite-volume numerical model using a non-orthogonal, algebraically generated adaptive grid was employed to solve the governing equations subject to the indicated boundary conditions. The development of the numerical model was more involved than simply a standard application of existing numerical techniques and deserves a more detailed treatment than space permits herein. A detailed description of the model, including its formulation and testing, a demonstration of its predictive capabilities for steady and unsteady problems, as well as a complete analysis of its sensitivity to the choice of numerical grid can be found in Haywood *et al.* [33] and Haywood [34].

RESULTS

The numerical model is used to calculate the early history of an *n*-heptane droplet evaporating in 1000 K air at 1 and 10 atmospheres ambient pressure. At both pressures, the droplet is initially spherical, uniform in temperature at 293 K and without internal or surface motion, and has an initial Reynolds number of 100 and a Weber number of 2 based on free stream thermophysical properties. The high pressure conditions are characteristic of larger droplets in hydrocarbon fuel sprays and would correspond, for example, to a 100 μm diameter droplet with an initial velocity of 10 m s^{-1}. For consistency, the same parameters ($We_{\infty,0}=2$, $Re_{\infty,0}=100$) are used for the low pressure problem; however, these conditions are admittedly less likely to be encountered in practice.

The transient histories of the aspect ratios, velocity, mass ratio, and liquid heating fraction are shown in Fig. 2(a) and (b) for the high and low pressure cases, respectively. Curves 1 show that droplets become initially flattened into oblate shapes with maximum aspect ratios of $\alpha=1.45$ (high pressure) and $\alpha=1.41$ (low pressure). The droplet at high ambient pressure displays only a single complete oblate/prolate oscil-

lation and temporarily settles into a prolate shape of aspect ratio of about 0.7 and then experiences a slow return to a slightly oblate shape ($\alpha = 1.07$). At low pressure, the droplet undergoes two complete oblate/prolate oscillations followed by three prolate/less-prolate oscillations and eventually settles into a prolate shape of aspect ratio $\alpha = 0.5$. The initial oscillation frequencies, based on the time elapsed between the first and second peaks of the aspect ratio histories, are found to be $\omega = 0.0100$ and 0.0244 at 1 and 10 atmospheres, respectively. These are less than the predictions of Lamb [13] for natural frequencies of inviscid oscillating droplets by 2 and 25%, respectively. The overprediction of the Lamb [13] solution is not surprising: the oscillation frequency will be reduced by the effects of both the finite oscillation amplitude and finite liquid and gas viscosities.

The viscous creeping flow analysis of Subramanyam [15] predicts $\omega = 0.0089$ and 0.0281 at 1 and 10 atmospheres, respectively. As seen in Fig. 2, the initial oscillations are quickly damped. At high pressure, the initial oscillations are over at approximately $t = 100$, at which time the droplet possesses 98.1% of its initial mass (curve 2). The corresponding values at low ambient pressure are $t = 500$ and $m/m_0 = 97.7$. At both ambient pressure levels the rate of damping is so large that the droplets are only affected by transient oscillations during a very small fraction of their total lifetimes. In spite of adequately predicting the oscillation frequency, the theoretical analysis of Subramanyam [15] underestimates the damping rate by about an order of magnitude; the theoretically predicted dimensionless times at which the initial distortions are damped to within 10% of their initial amplitudes are $t = 700$ and 6000 at high and low pressure, respectively.

Two unexpected trends are observed in the present predicted behavior of the transient deforming droplet: (1) the formation of prolate shapes in contrast to experimental results (e.g. Garner and Lane [24]) which demonstrate oblate shapes exclusively, and (2) an extremely high rate of damping. As described below, the shear driven motion within the liquid phase is the physical mechanism responsible for both of these phenomena.

The observed liquid phase motion can be generally described as the superposition of the fluid flow generated by an oblate/prolate oscillation with that of an internal toroidal vortex. Because the droplets are assumed to be initially motionless internally, the former dominates during the earliest portion of the droplet life but is quickly supplanted by the rapid growth of the internal circulation. Figure 3 shows velocity vector plots within the liquid phase during the early history of the high pressure case ($t = 7$, 15, 23 and 150). In the first two frames ($t = 7$, 15), the droplet is becoming increasingly oblate and a general trend of inward flow at the leading and trailing stagnation regions is observed. The spherical vortex is beginning

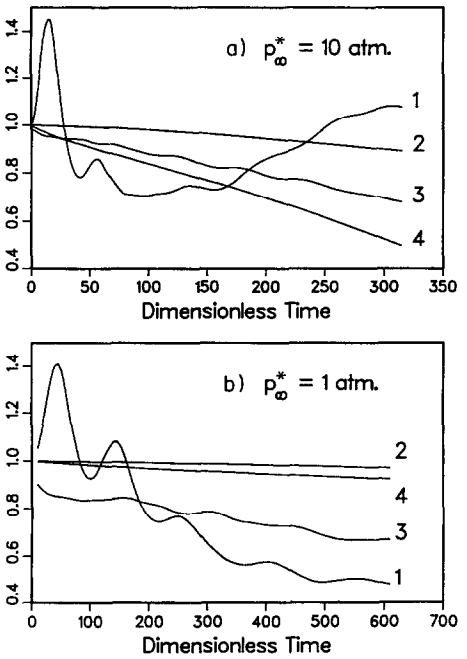

FIG. 2. Overall results: (a) $p^*_\infty = 10$ atm, (b) $p^*_\infty = 1$ atm; (1) aspect ratio α; (2) mass m/m_0; (3) liquid heating fraction Q_l/Q_g; (4) velocity $U^*_\infty/U^*_{\infty,0}$.

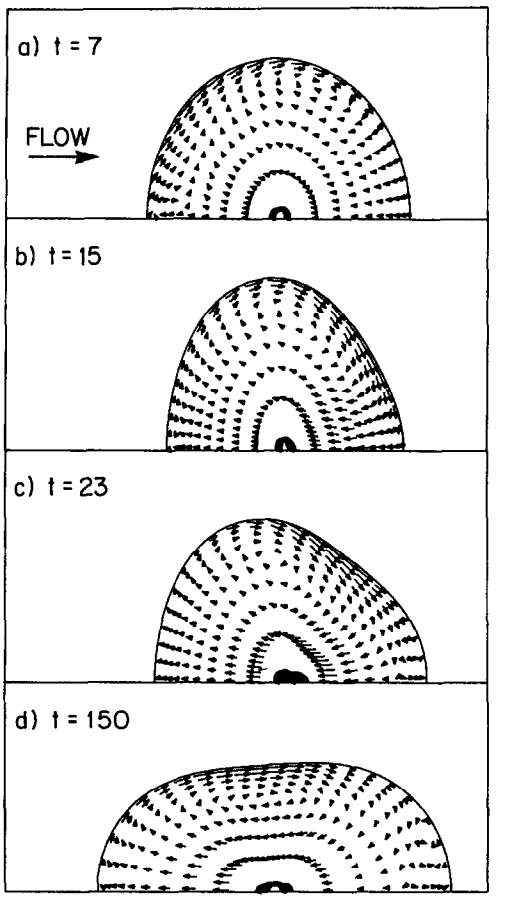

FIG. 3. Liquid phase velocity field, $p^*_\infty = 10$ atm.

to form, its center near the liquid/gas interface just aft of the droplet center, its maximum velocity approximately 10% of the initial free stream velocity. In the third frame ($t = 23$), the droplet is rebounding from the first oblate excursion and the flow due to oscillation has reversed such that the flow is now from the droplet equator towards the stagnation regions. The liquid circulation is better developed with a maximum velocity now 14% of $U_{\infty,0}$, and augments the flow towards the trailing stagnation region while interfering with the flow to the leading stagnation region. The resulting droplet is considerably fore–aft asymmetric. The fourth frame ($t = 150$), shows that the liquid motion due to the initial oscillations has decayed. A stable internal circulation pattern has developed with a maximum velocity of $0.128U_{\infty,0}$. The internal circulation generates high pressure regions at the fore and aft stagnation points and a low pressure region at the drop equator. The droplet has assumed a prolate shape as a result. In studies of raindrops, Foote [31] predicted that the effect of internal circulation is to oppose droplet flattening, that is, oblate shapes. In the absence of a mechanism tending to reduce internal circulation, such as surface active agents, hydrocarbon droplets evaporating in air are strongly influenced by liquid phase circulation aided by the low liquid to gas viscosity ratio, and the high density ratio. Unless extreme precautions are taken, all engineering systems (including experimental facilities) are contaminated with surfactants, which explains why prolate shapes are not observed in practice.

In the present study, both free-surface and variable-property effects are included. The concurrent action of these gives rise to the Marangoni effect, that is, interfacial shear stress due to variations in surface tension. Figure 4 shows the magnitudes of the terms appearing in the tangential stress balance due to the gas phase shear, the liquid phase shear, and the Marangoni stresses at $t = 23$ and 315 for the high pressure droplet. In both cases, the Marangoni stress and the gas phase shear stress are of equal magnitude. However, unlike the gas phase shear which is at all times consistent in its action, at early times the Marangoni stress is dependent on a highly variable interfacial temperature distribution. This distribution is a result of the large thermal inertia of the liquid phase coupled with its uneven heating and mixing due to circulation and oscillation. The resulting Marangoni stress therefore does not initially contribute to the liquid motion in a coherent manner. The surface temperature distribution of the high pressure droplet eventually settles into a generally increasing trend along the surface and consequently the Marangoni stress acts to reduce the surface motion. At $t > 250$, the reduction in circulation strength allows the droplet to return to an oblate shape.

The normal stresses acting on the liquid phase are shown in Fig. 5 at time $t = 23$ for the high pressure droplet. At all times, the normal viscous stresses

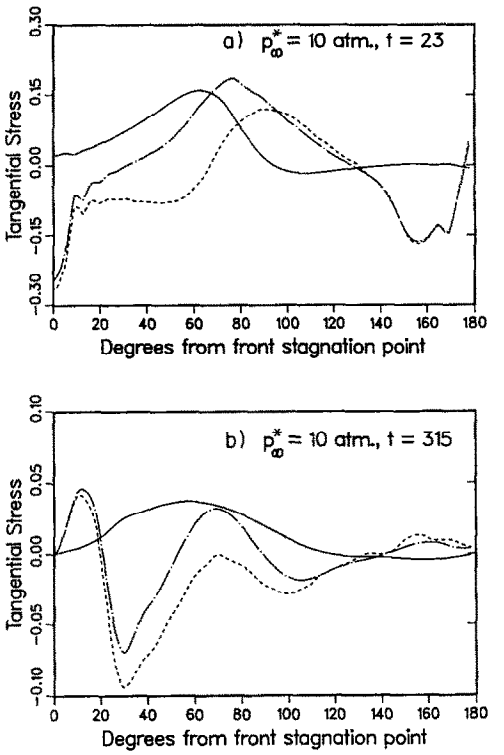

FIG. 4. Interface tangential stresses, $p^*_\infty = 10\,\text{atm}$; (a) $t = 23$; (b) $t = 315$; —— $(2/Re_{\infty,0})(\vec{\sigma}\cdot\hat{n}\cdot\hat{t})_g$; —·— $(2/Re_{\infty,0})(\vec{\sigma}\cdot\hat{n}\cdot\hat{t})_l$; – – – $(2/We_{\infty,0})\vec{\nabla}_s\gamma\cdot\hat{t}$.

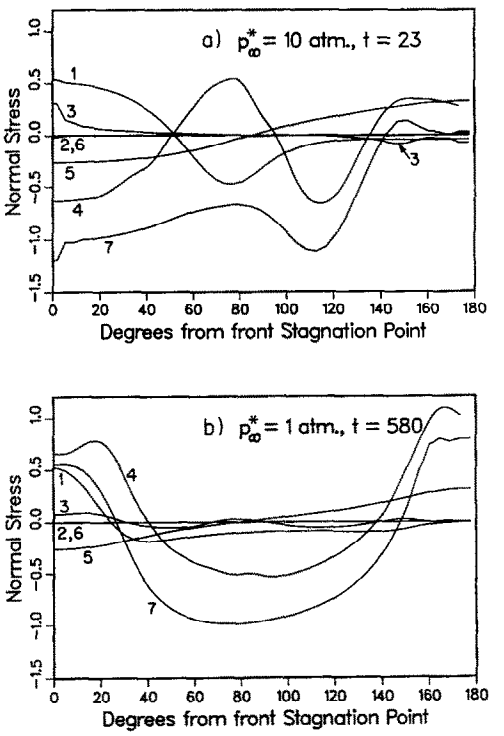

FIG. 5. Interface normal stresses, (a) $p^*_\infty = 10\,\text{atm}$, $t = 23$; (b) $p^*_\infty = 1\,\text{atm}$, $t = 580$; (1) p^*_g; (2) $(-2/Re_{\infty,0})(\vec{\sigma}\cdot\hat{n}\cdot\hat{n})_g$; (3) $(-2/Re_{\infty,0})(\vec{\sigma}\cdot\hat{n}\cdot\hat{n})_l$; (4) $(-4(\gamma H+1)/We_{\infty,0})$; (5) $-\rho_l x\,dU_\infty/dt$; (6) $\dot{m}''(\vec{v}_g-\vec{v}_l)\cdot\hat{n}$; (7) p^*_l.

(curves 2 and 3) and the normal stress due to mass flow across the interface (curves 6) are practically insignificant. Although the liquid heating is inhibiting the full effect of evaporation, the numerical data show that the stress due to evaporation is typically 3 orders of magnitude smaller than the other major terms in the stress balance at the time shown. Even for highly volatile fuels it is unlikely that droplet shapes will be directly affected significantly by the normal stress due to evaporation. The normal stress balance is dominated by the gas phase pressure (curves 1), the pressure within the droplet due to the droplet deceleration (curves 5), the liquid phase pressure (curves 7), and the surface tension induced normal stress (curves 4).

The sensitivity of the heat, mass, and momentum transfer rates to the interface motion is now investigated. In view of the observed disparity between the interface and free stream velocities one would expect the interface motion to have negligible effect. Indeed, Clift *et al.* [12] suggest that no effect due to droplet oscillation is expected when $\omega < 0.075$. Figure 6 shows the numerical results and the corresponding quasi-steady predictions based on correlations given below for the Nusselt and Sherwood numbers at high and low ambient pressures. The numerical results show initial oscillations in the Sherwood number history, and to a lesser extent in the Nusselt number history. A comparison of Fig. 6(a) and (b) with Fig. 2 shows that these oscillations are in phase with the oscillations in the aspect ratio history. Furthermore, in studies of transfer rates from spheroids, Masliyah and Epstein [35] and Chuchottaworn and Asano [36] report that transfer rates increase with increasing aspect ratio. It therefore seems likely that the initial oscillations are a direct result of the changing droplet shape and not due to the interfacial motion itself. Figures 6 also shows that the following correlations (Renksizbulut and Yuen [37], Haywood *et al.* [9], Renksizbulut *et al.* [38]) can be used in a quasi-steady manner to predict Nu_∞, and Sh_∞ within 8% of the numerical data, provided that the correlations are based on the droplet volume equivalent diameter:

$$Nu_f(1+B_{H,f})^{0.7} = 2+0.57Re_m^{1/2}Pr_f^{1/3}; \quad 20 \leqslant Re_m \leqslant 2000 \quad (14)$$

$$Sh_f(1+B_M)^{0.7} = 2+0.87Re_m^{1/2}Sc_f^{1/3}; \quad 10 \leqslant Re_m \leqslant 2000. \quad (15)$$

Figure 7 shows the drag coefficient histories at both pressure levels based on the instantaneous frontal area of a volume equivalent sphere. The observed trends are consistent with the aspect ratio histories given in Fig. 2. Figure 7 also shows that C_D can be predicted with good accuracy (within 12%) using:

$$C_D = C_D^* A_{frontal}/A_{equivalent} \quad (16)$$

where $A_{frontal}$ is the actual frontal area of the deformed droplet, $A_{equivalent}$ is the frontal area of a volume equivalent droplet, and C_D^* is given by the drag correlation of Renksizbulut and Yuen [6] (see also Haywood *et al.* [9]) for evaporating spherical droplets:

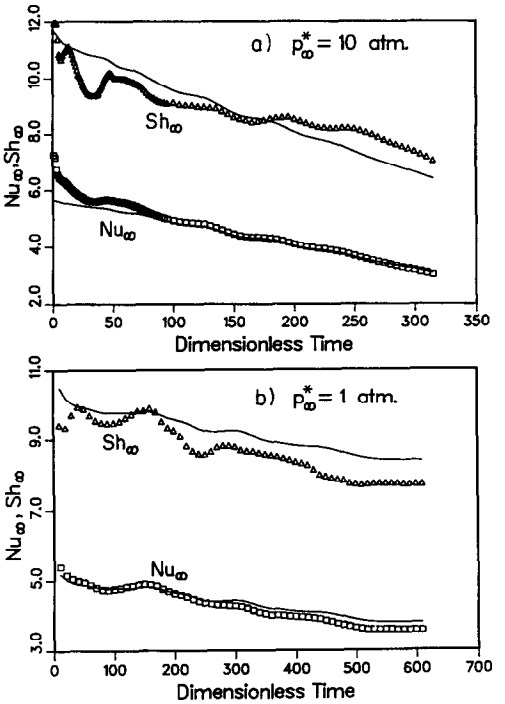

FIG. 6. Nusselt and Sherwood number histories, (a) $p_\infty^* = 10$ atm, (b) $p_\infty^* = 1$ atm; symbols = numerical data; —— equations (14) and (15).

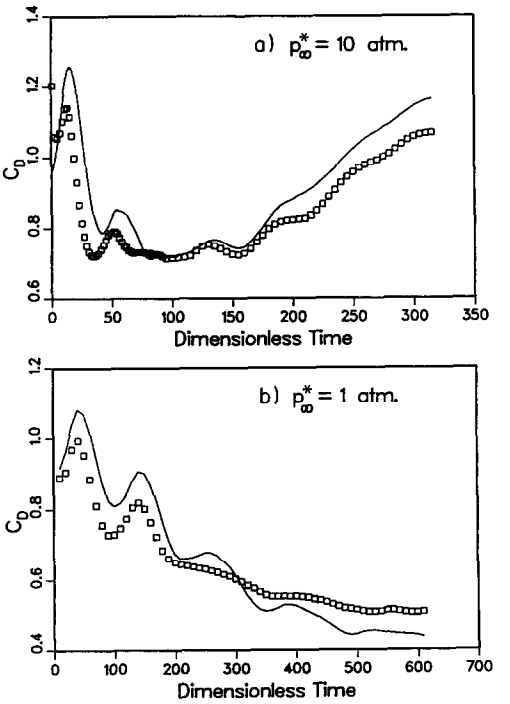

FIG. 7. Drag coefficient history, (a) $p_\infty^* = 10$ atm, (b) $p_\infty^* = 1$ atm; □ numerical data; —— equation (16).

$$C_D^*(1+B_{H,f})^{0.2} = \frac{24}{Re_m}(1+0.2Re_m^{0.63}); \quad 10 \leqslant Re_m \leqslant 300. \quad (17)$$

There is unfortunately no simple way of determining the instantaneous frontal area of a deforming droplet at the present time, which severely limits the usefulness of equation (16).

Transient surface motion has been observed to have little effect on the gas phase transfer processes. However, it is possible that the effect of interface motion on the liquid phase behavior may be of greater consequence because the magnitudes of the interface and liquid-phase velocities are much closer. To understand the liquid heating behavior of deforming droplets, a liquid phase Nusselt number is defined following Johns and Beckmann [39]:

$$Nu_l = \left(\frac{m}{m_o}\right)^{1/3} \frac{1}{(\bar{T}_s - \bar{T}_l)} \frac{\int_S k\vec{\nabla}T\cdot\hat{n}\,dA}{\int_S k\,dA}. \quad (18)$$

Figure 8 shows the transient history of the liquid Nusselt number, and for reference the aspect ratio. Generally, the trends are what would be expected for the transient high Peclet number behavior as predicted by Johns and Beckmann [39]; namely the oscillatory approach to an asymptotic limiting value of $Nu_l \approx 20$. The Nu_l oscillations are a result of the low liquid-phase thermal diffusivity coupled with initial conditions that generate an internal vortex with distinct cold (initially internal) and warm (initially surface) regions. As verification, the oscillation time should equal the circulation time of the internal vortex. The circulation time is simply estimated as the distance across the surface from front to rear stagnation points, plus the direct distance from front to rear stagnation points, divided by the circulation velocity taken to be an average tangential surface velocity. For the high pressure case, the expected circulation period is $(\pi+2)R_o^*/(0.1U_{\infty,o}^*) \approx 51$. Allowing for some variation in the circulation distance and velocity, the liquid Nusselt number shows oscillations reasonably close to this periodicity for all but the earliest oscillations ($t < 70$). It appears that the early liquid heating behavior is affected by the interface motion. Close examination of the liquid phase temperature field shows a warm pocket of fluid trapped during the first oblate/prolate oscillation ($t < 15$). The high initial liquid Nusselt numbers are a result of cold internal fluid being forced to the leading stagnation region due to the liquid circulation. When the warm fluid pocket arrives, a decline in Nu_l results ($45 < t < 60$). As the warm pocket passes and new colder fluid is again forced to the surface, Nu_l again rises. Beyond this initial interaction, the interface motion is damped and no further effect of interface motion on liquid heating is observed. At the low ambient pressure, a similar behavior is observed but the effect is less pronounced due to the reduced oscillation frequency. Once again, for combustion problems the limited duration of the oblate/prolate shape oscillations minimizes the impact of interface motion on the overall liquid phase heat transfer. Nevertheless, during the limited period of interaction it appears that shape oscillations result in enhanced mixing.

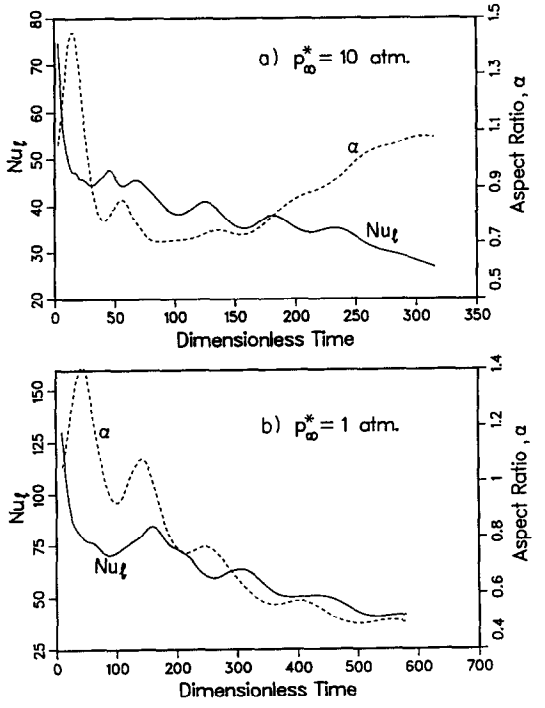

FIG. 8. Liquid Nusselt number history, (a) $p_\infty^* = 10$ atm, (b) $p_\infty^* = 1$ atm; —— equation (18); – – – aspect ratio.

CONCLUSIONS

The initial oscillations of fuel droplets at 1 and 10 atmospheres ambient pressure occur at frequencies within 25% of the natural frequency predicted by Lamb [13]. Significant liquid phase motion causes droplets to elongate into prolate shapes. The liquid motion opposes the natural oblate/prolate oscillations of the droplets and strongly damps the initial oscillations.

The quasi-steady correlations for Nusselt and Sherwood numbers based on the instantaneous volume equivalent diameter adequately predict the rates of heat and mass transfer for unsteady deformed droplets. The quasi-steady drag correlation based on the instantaneous projected frontal area also adequately predicts the aerodynamic drag on the droplets.

Acknowledgements—This work was made possible through financial assistance from the Natural Sciences and Engineering Research Council of Canada, the Government of Ontario, the Manufacturing Research Council of Ontario, and the Carl Pollock Foundation.

REFERENCES

1. C. K. Law, Recent advances in droplet vaporization and combustion, *Prog. Energy Combust. Sci.* **8**, 171–201 (1982).

2. G. M. Faeth, Evaporation and combustion of sprays, *Prog. Energy Combust. Sci.* **9,** 1–76 (1983).
3. W. A. Sirignano, Fuel droplet vaporization and spray combustion theory, *Prog. Energy Combust. Sci.* **9,** 291–322 (1983).
4. H. A. Dwyer, Calculations of droplet dynamics in high temperature environments, *Prog. Energy Combust. Sci.* **9,** 1–76 (1989).
5. S. Prakash and W. A. Sirignano, Theory of convective droplet vaporization with unsteady heat transfer in the circulating liquid phase, *Int. J. Heat Mass Transfer* **23,** 253–268 (1980).
6. M. Renksizbulut and M. C. Yuen, Numerical study of droplet evaporation in a high-temperature air stream, *J. Heat Transfer* **105,** 389–397 (1983).
7. H. A. Dwyer and B. R. Sanders, Detailed computation of unsteady droplet dynamics, *Twentieth Symposium (International) on Combustion*, The Combustion Institute, pp. 1743–1749 (1984).
8. M. Renksizbulut and R. J. Haywood, Transient droplet evaporation with variable properties and internal circulation at intermediate Reynolds numbers, *Int. J. Multiphase Flow* **14,** 189–202 (1988).
9. R. J. Haywood, R. Nafziger and M. Renksizbulut, A detailed examination of gas and liquid phase transient processes in convective droplet evaporation, *J. Heat Transfer* **111,** 495–502 (1989).
10. L. Huang and P. S. Ayyaswamy, Evaporation of moving liquid droplet : solutions for intermediate Reynolds numbers, *Int. Comm. Heat Mass Transfer* **17,** 27–38 (1990).
11. C. H. Chiang, M. S. Raju and W. A. Sirignano, Numerical analysis of convecting, vaporizing fuel droplet with variable properties, *Int. J. Heat Mass Transfer* **35,** 1307–1324 (1992).
12. R. Clift, J. R. Grace and M. E. Weber, *Bubbles, Drops and Particles*, Chaps. 7 and 8. Academic Press, New York (1978).
13. H. Lamb, *Hydrodynamics*, Chap. 9. Dover Publications, New York (1932).
14. C. A. Miller and L. E. Scriven, The oscillations of a fluid droplet immersed in another fluid, *J. Fluid Mech.* **32**(3), 417–435 (1968).
15. S. V. Subramanyam, A note on the damping and oscillations of a fluid drop moving in another fluid, *J. Fluid Mech.* **37**(4), 715–725 (1969).
16. J. F. Harper, The motion of bubbles and drops through liquids, *Adv. Appl. Mech.* **12,** 59–129 (1972).
17. M. Miksis, J. M. Vanden-broeck and J. B. Keller, Axisymmetric bubble or drop in a uniform flow, *J. Fluid Mech.* **108,** 89–100 (1981).
18. G. Ryskin and L. G. Leal, Numerical solution of free-boundary problems in fluid mechanics. Part 1 : The finite-difference technique, *J. Fluid Mech.* **148,** 1–17 (1984).
19. C. I. Christov and K. Volkov, Numerical investigation of the steady viscous flow past a stationary deformable bubble, *J. Fluid Mech.* **158,** 341–364 (1985).
20. D. S. Dandy and L. G. Leal, Buoyancy-driven motion of a deformable drop through a quiescent liquid at intermediate Reynolds numbers, *J. Fluid Mech.* **208,** 161–192 (1989).
21. Z.-T. Deng, R. Litchford, S. Jeng and S.-M. Jeng, Two dimensional simulations of droplet evaporation and deformation at high pressure, *AIAA* 92-3122, *AIAA/SAE/ASME/ASEE 28th Joint Propulsion Conference and Exhibit*, 6–8 July, Nashville, TN (1992).
22. J. R. Grace, Shapes and velocities of bubbles rising in infinite liquids, *Trans. Instn Chem. Engrs* **51,** 116–120 (1973).
23. J. R. Grace, T. Wairegi and T. H. Nguyen, Shapes and velocities of single drops and bubbles moving freely through immiscible liquids, *Trans. Instn Chem. Engrs* **54,** 167–173 (1976).
24. F. H. Garner and J. J. Lane, Mass transfer to drops of liquid suspended in a gas stream. Part II : Experimental work and results, *Trans. Instn Chem. Engrs* **37,** 162–172 (1959).
25. S. Winnikow and B. T. Chao, Droplet motion in purified systems, *Phys. Fluids* **9**(1), 50–61 (1966).
26. G. Thorsen, R. M. Stordalen and S. G. Terjesen, On the terminal velocity of circulating and oscillating liquid drops, *Chem. Engng Sci.* **23,** 413–426 (1968).
27. C. Magono, On the shape of water drops falling in stagnant air, *J. Meteor.* **11,** 77–79 (1954).
28. J. E. McDonald, The shape and aerodynamics of large raindrops, *J. Meteor.* **11,** 478–494 (1954).
29. A. Reinhart, Das Verhalten Fallender Tropfen, *Chemie-Ing.-Techn.* **36**(7), 740–746 (1964).
30. H. R. Pruppacher and K. V. Beard, A wind tunnel investigation of the internal circulation and shape of water drops falling at terminal velocity in air, *Quart. J. R. Met. Soc.* **96,** 247–256 (1970).
31. G. B. Foote, On the internal circulation and shape of large raindrops, *J. Atmos. Sci.* **26,** 179–181 (1969).
32. A. G. Petrov, Internal circulation and deformation of viscous drops, *Vestnik Moskovskogo Universiteta. Mekhanika* **43**(3), 85–88 (1988).
33. R. J. Haywood, M. Renksizbulut and G. D. Raithby, Numerical solution of deforming evaporating droplets at intermediate Reynolds numbers, *Numerical Heat Transfer, Part A : Applications*, accepted, November 1993.
34. R. J. Haywood, Dynamics and energetics of deformable evaporating droplets at intermediate Reynolds numbers, Ph.D. Thesis, University of Waterloo, Waterloo, Ontario, Canada (1992).
35. J. H. Masliyah and N. Epstein, Numerical solution of heat and mass transfer from spheroids in steady axisymmetric flow, *Prog. Heat Mass Transfer* **6,** 613–632 (1972).
36. P. Chuchottaworn and K. Asano, Numerical analysis of drag coefficients and the heat and mass transfer of spheroidal drops, *J. Chem. Eng. Japan* **19**(3), 208–213 (1986).
37. M. Renksizbulut and M. C. Yuen, Experimental study of droplet evaporation in a high-temperature air stream, *J. Heat Transfer* **105,** 384–388 (1983).
38. M. Renksizbulut, R. Nafziger and X. Li, A mass transfer correlation for droplet evaporation in high temperature flows, *Chem. Engng Sci.* **46,** 2351–2358 (1991).
39. L. E. Johns, Jr. and R. B. Beckmann, Mechanism of dispersed-phase mass transfer in viscous, single-drop extraction systems, *A.I.Ch.E. Jl* **12,** 10–16 (1966).